batteries

MDPI

Article

Facile Constructing Hierarchical Fe_3O_4@C Nanocomposites as Anode for Superior Lithium-Ion Storage

Haichang Zhong [1], Wenlong Huang [1], Yukun Wei [1,3], Xin Yang [2], Chunhai Jiang [1], Hui Liu [2,*], Wenxian Zhang [1], Chu Liang [4], Leyang Dai [3] and Xijun Xu [5,*]

1 Fujian Provincial Key Laboratory of Functional Materials and Applications, School of Materials Science and Engineering, Xiamen University of Technology, Xiamen 361024, China; 2013204215@s.xmut.edu.cn (W.H.); max@jmu.edu.cn (Y.W.); chjiang@xmut.edu.cn (C.J.); wxzhang@xmut.edu.cn (W.Z.)
2 School of Chemistry and Material Science, Hunan Agricultural University, Changsha 410128, China; xinyang@stu.hunau.edu.cn
3 School of Marine Engineering, Jimei University, Xiamen 361021, China; daileyang@jmu.edu.cn
4 College of Materials Science and Engineering, Zhejiang University of Technology, Hangzhou 310014, China
5 College of Chemical Engineering and Light Industry, Guangdong University of Technology, Guangzhou 510006, China
* Correspondence: liu.hui@hunau.edu.cn (H.L.); xuxijun2022@gdut.edu.cn (X.X.)

Abstract: Ferroferric oxide (Fe_3O_4) is regarded to be a promising high-capacity anode material for LIBs. However, the capacity attenuates fast and the rate performance is poor due to the dramatic pulverization and sluggish charge transfer properties. To solve these problems, a simple in situ encapsulation and composite method was successfully developed to construct carbon nanotube/nanorod/nanosheet-supported Fe_3O_4 nanoparticles. Owing to the hierarchical architecture design, the novel structure Fe_3O_4@C nanocomposites effectively enhance the charge transfer, alleviate pulverization, avoid the agglomeration of Fe_3O_4 nanoparticles, and also provide superior kinetics toward lithium storage, thereby showing significantly improved reversibility and rate performance. The carbon nanotube/nanorod supported core-shell structure Fe_3O_4@C nanocomposite displays outstanding high rate capability and stable cycling performance (reversible capability of 1006, 552 and 423 mA h g^{-1} at 0.2, 0.5 and 1 A g^{-1} after running 100, 300 and 500 cycles, respectively).

Keywords: Fe_3O_4@C nanocomposites; anode; lithium-ion batteries; hierarchical structure; nanocomposite

check for updates

Citation: Zhong, H.; Huang, W.; Wei, Y.; Yang, X.; Jiang, C.; Liu, H.; Zhang, W.; Liang, C.; Dai, L.; Xu, X. Facile Constructing Hierarchical Fe_3O_4@C Nanocomposites as Anode for Superior Lithium-Ion Storage. *Batteries* **2023**, *9*, 403. https://doi.org/10.3390/batteries9080403

Academic Editor: Hirotoshi Yamada

Received: 26 June 2023
Revised: 12 July 2023
Accepted: 27 July 2023
Published: 2 August 2023

Copyright: © 2023 by the authors. Licensee MDPI, Basel, Switzerland. This article is an open access article distributed under the terms and conditions of the Creative Commons Attribution (CC BY) license (https://creativecommons.org/licenses/by/4.0/).

1. Introduction

The lithium-ion battery (LIB), an effective energy storage device, is extensively applied to electric vehicles and various portable devices, e.g., mobile phones, laptops and so on [1–3]. However, commercial graphite as an anode material has fatal disadvantages of low specific capacity (372 mAh g^{-1}) and deficient rate performance, so the present LIB cannot support sufficient capacity for intelligent electronic devices to satisfy people's demand for long working time [1,4]. To solve the problem, we need to explore new suitable anode materials with high specific capacity and excellent cycling stability. In the past decades, intensive efforts have been employed to explore various kinds of new anode materials, including Si, Sn, NiSb, etc.; alloy-type [5–9] and transition metal oxides (e.g., Fe_2O_3/Fe_3O_4, Co_3O_4, SnO_2, etc.) [10–14] and so on. Ferroferric oxide (Fe_3O_4) is regarded to be a promising anode material and attracts many researchers' interest due to the merits of high reversible theoretical specific capacity (928 mAh g^{-1}), low cost and eco-friendliness [9,10,15–17]. Unfortunately, the capacity of the Fe_3O_4 anode decays very fast, which results from the severe pulverization of Fe_3O_4 particles because of the huge volume variation caused by lithiation and delithiation; therefore, the Fe_3O_4 anode exhibits poor cycling stability [18–21]. On the other hand, the charge transfer property of the pristine Fe_3O_4 is poor and needs to be improved in an electrode material [22,23].

To solve these disadvantages, many strategies were explored to enhance the structural stability and improve the electrical conductivity of Fe_3O_4 [23–27]. Concerning enhancing the structural stability, the synthesis of nanostructured Fe_3O_4, such as nanoparticles, nanorods, hollow spheres, and so on, was intensively investigated [24–29]. The other way is designing Fe_3O_4@C nanocomposites, including carbon-coated Fe_3O_4 nanocomposites [16], graphene-wrapped nano-Fe_3O_4 or 3D structured Fe_3O_4@C nanocomposites [30–32]. Compared with the bulk Fe_3O_4, nanostructured Fe_3O_4 is not only beneficial in alleviating the stress but also helps to reduce the Li/Li^+ diffusion distance [33–35]. It was reported that the single-crystalline Fe_3O_4 and α-Fe_2O_3 nanorods could alleviate stress effectively and supply a larger electrochemical reaction area [36]. With respect to Fe_3O_4@C nanocomposites, the carbon matrix severed as a buffer for the accommodation of strain and inhibited the agglomeration and coarsening of nano-Fe_3O_4 [37]. On the other hand, attributed to its good conductivity, the introduction of carbon also enhances the charge transfer of Fe_3O_4 [38]. As a result, the Fe_3O_4@C nanocomposites always display improved cycling stability. For example the Fe_3O_4 nanoparticles encapsulated by macroporous carbon spheres exhibited a discharge capacity of 645 mAh g^{-1} after 1000 cycles at 2.0 A g^{-1} [28].

Recently, constructions of yolk-shell or other hollow structures became a favorable methodology to realize the special structural effects [39–42]. Metal–organic frameworks (MOFs) were considered to be the ideal precursors for the preparation of functional porous materials (metal/metal oxide and carbon composites) with desired shapes [17,41,43,44]. Using ferrocene as the precursor, Liu and co-authors synthesized a pitaya-structured Fe_3O_4@C nanocomposite and finally obtained the same structured FeS_2@C nanocomposites as a cathode material for LIBs, which displayed stable and high energy density (~1100 Wh kg^{-1}) and ultrahigh rate capability41. The yolk-shell Fe_2O_3@C composite containing mesoporous derived from MIL-53(Fe), could retain 744 mAh g^{-1} after 500 cycles at 1 A g^{-1} [43] Although notable successes have been achieved, these chemical synthesis methods were severely limited by their multistep, the use of organic solvents and low yield [45] In this work, we presented a facile and suitable large-scale application method to prepare Fe_3O_4@C nanocomposites with controllable morphologies by carbonizing the plasma-assisted ball-milled ferrocene ($C_{10}H_{10}Fe$) precursor. The leaves-like amorphous carbon-nanosheet-encapsulated ultrafine nano-Fe_3O_4 and carbon nanotubes/nanorods-supported core-shell nanostructured Fe_3O_4 composites were prepared and exhibited outstanding electrochemical performances as an anode material for LIBs. Typically the carbon nanotubes/nanorods-supported core-shell nanostructured Fe_3O_4 presented impressive cycling performance (423 mAh g^{-1} at 1 A g^{-1} after 500 cycles) and outstanding high-rate capability.

2. Experiments

2.1. Material Preparation and Characterization

The synthesis of Fe_3O_4@C nanocomposites is illustrated in Scheme 1. First, the purchased ferrocene ($C_{10}H_{10}Fe$) powders were milled for 5 h on a plasma-assisted ball miller (PA miller, homemade) to achieve partially carbonized pretreated products. Then, these pretreated products were annealed in the tube furnace at 773 and 873 K for 30 min under the atmosphere of argon and air mixtures. The obtained black powders were the final Fe_3O_4@C nanocomposites. The Fe_3O_4@C nanocomposites achieved at 773 and 873 K were named Fe_3O_4@C-773 and Fe_3O_4@C-873, respectively, in the following.

The phase components of the Fe_3O_4@C composites were examined by an X-ray diffractometer (XRD, Rigaku SmartLab 2 kW, Tokyo, Japan) using Cu-Kα radiation (λ = 1.54056 Å) at 40 kV and 40 mA. The morphology and microstructure were further investigated by a field emission scanning electron microscope (SEM, ZEISS Sigma 500) and scanning transmission electron microscopy (STEM, FEI TALOS F200S attached BRUKER Super-X EDS). The carbon contents were determined using thermogravimetric analysis (TG, Setaram Labsys) at a heating rate of 2 K/min under an airflow of 50 mL/min. The pore structure and specific surface area were evaluated by the measurement of nitrogen adsorption/desorption

isotherms at 77 K on a micromeritics 3Flex instrument (USA). The Raman spectra were tested on an invia apparatus (Renishaw, Wotton-under-Edge, UK). X-ray photoelectron spectroscopy (XPS, Nexsa from ThermoFisher Inc., Waltham, MA, USA) was performed to analyze the chemical components and element valance.

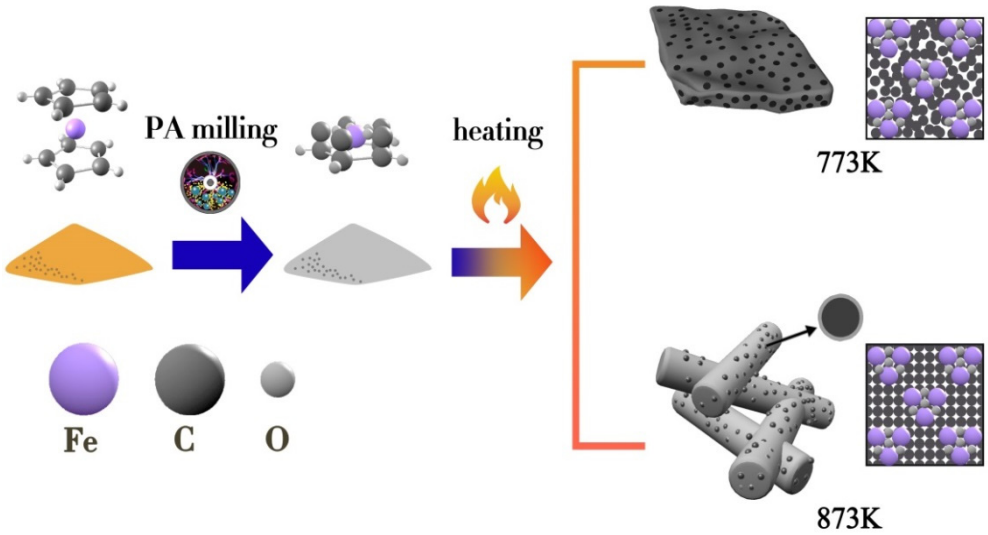

Scheme 1. Schematic illustration of the preparation of the Fe_3O_4@C nanocomposites.

2.2. Electrochemical Measurements

The slurry was obtained by grinding the Fe_3O_4@C composites, binder-polyvinylidene fluoride (PVDF) and conductive additive (Super P) with a weight ratio of 8:1:1 in a mortar with an appropriate Nmethyl-2-pyrrolidone (NMP) on a ball mill. The prepared slurry was coated on the Cu foil, which then was dried at 85 °C for 24 h under vacuum conditions. The button batteries (Li//Fe_3O_4@C) were assembled in a glove box under the protection of high-purity Ar (O_2 and H_2O < 0.1 ppm). Lithium metal was the cathode, a celgard2400 membrane was the separator and a solution of 1 M $LiPF_6$ dissolved in ethylene carbonate and diethyl carbonate (1:1 in volume) was the electrolyte. The galvanostatic charge/discharge measurements were performed on a LAND-CT2001A battery test system in the voltage range from 0.1 to 3.0 V (vs. Li/Li^+). A CHI660D electrochemical workstation was used for the measurements of cyclic voltammetry (CV) profiles in a voltage range of 0.01 to 3.0 V by a scan rate of 1 mV s^{-1}, and electrochemical impedance spectroscopy (EIS) was used from 100 kHz to 0.1 Hz.

3. Results and Discussion

Figure 1a shows the XRD patterns of the Fe_3O_4@C nanocomposites. The diffraction peaks at 18.3°, 30.0°, 35.3°, 43.1°, 57.0° and 62.5° match well with the (111), (220), (311), (400), (333) and (440) crystal plane diffractions of Fe_3O_4, respectively. This result indicated that Fe_3O_4 crystalline was formed by sintering the PA-milled $C_{10}H_{10}Fe$ at 773 and 873 K for 30 min. The diffraction intensities of Fe_3O_4 in Fe_3O_4@C-873 were comparatively higher than these of Fe_3O_4@C-773, which could result from the better crystallinity due to the higher annealing temperature for Fe_3O_4@C-873. On the other hand, the (002) peak of carbon (JCPDS no. 89-7213) was confirmed in Fe_3O_4@C-873. However, there was no observed carbon diffraction peak in Fe_3O_4@C-773, which could be attributed to its amorphous structure. Figure 1b shows the TG results for two samples. From Figure 1b, it could be seen that the major weight loss, induced by the removement of carbon due to oxidation, occurred at approximately 750 K. The weight loss starting temperature of Fe_3O_4@C-773 was obviously lower than that of Fe_3O_4@C-873. This could be because the amorphous carbon was more easily oxidated in the air condition. The weight percent of carbon was approximately 29 wt.% and 8 wt.% for Fe_3O_4@C-773 and Fe_3O_4@C-873, respectively, based

on the TG results. It implied that the higher annealing temperature would result in more weight loss in carbon.

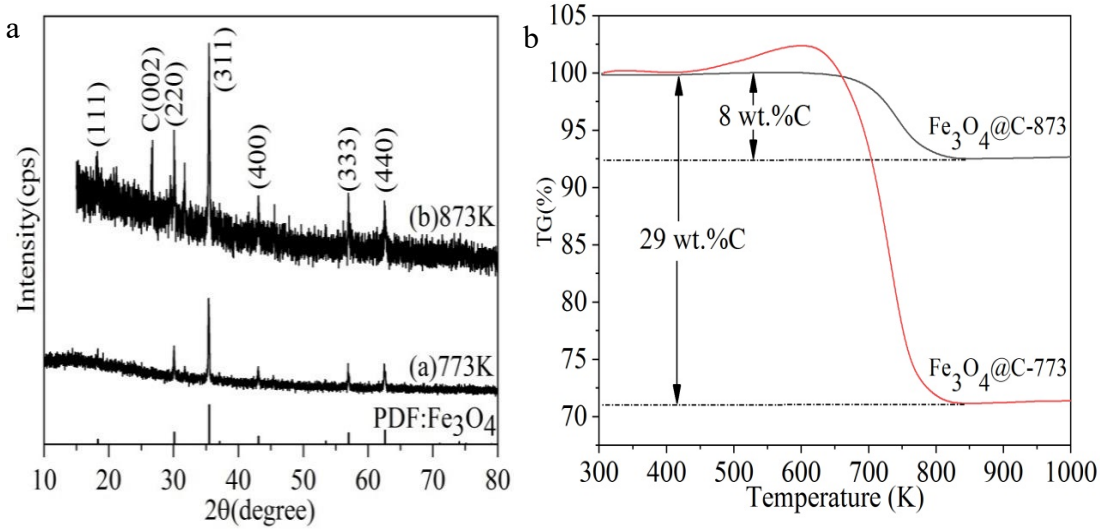

Figure 1. (**a**) XRD, (**b**) thermogravimetric analysis cures for Fe_3O_4@C composite.

Figure 2 shows the morphology and microstructure of the Fe_3O_4@C nanocomposites. Fe_3O_4@C-773 and Fe_3O_4@C-873 showed completely different morphologies. As observed in Figure 2a,b, Fe_3O_4@C-773 showed a leaves-like nanosheet structure with the Fe_3O_4 nanoparticles (~5 nm) dispersively embedded in the carbon leaves. The insert of Figure 2b is the STEM-selected area diffraction pattern, which contained an amorphous diffraction ring of carbon together with the (111) and (220) facet families of the polycrystalline Fe_3O_4. These agreed well with the above X-ray diffraction analysis results. Figure 2c is the enlarged image of the marked part in Figure 2a, and the related mapping for C, Fe, and O are illustrated in Figure 2d–f. The mapping results further confirmed that the ultrafine Fe_3O_4 nanoparticles were dispersively incorporated into the carbon matrix. Different from Fe_3O_4@C-773, Fe_3O_4@C-873 was characterized by a nanotube/nanorod structure and coated with larger Fe_3O_4 nanoparticles (~100 nm), as seen in Figure 2g (SEM) and Figure 2h (STEM). From the insert of Figure 2h, it could be clearly seen that the Fe_3O_4 nanoparticles were wrapped by a nanolayer of carbon (~5 nm) with a typical core-shell nanostructure. The core-shell structure could be more favorable for the release of strain caused by Li/Li^+ insertion/extraction, and the carbon matrix could serve as a buffer for the accommodation of stress resulting from the sharp volume variation in Fe_3O_4, thereby avoiding the severe pulverization of Fe_3O_4 [46]. It was regarded that this novel structure greatly benefitted the enhancement of the structural stability of nano-Fe_3O_4.

Figure 3a illustrates the Raman spectroscopies of the Fe_3O_4@C nanocomposites. Fe_3O_4@C-773 and Fe_3O_4@C-873 exhibited two bands, centering at approximately 1343 cm^{-1} and 1589 cm^{-1}, attributed to the D-band and G-band, respectively [47]. According to the references [17,48], the D-band was the characteristic peak of the disordered amorphous structure of carbon, and the G-band was attributed to the sp2 hybridization of carbon materials. Observably, the intensity of the D-band decreased with the increased annealing temperature of the Fe_3O_4@C composites. For Fe_3O_4@C-773, the larger value of I_D/I_G (>1) implied a higher density of defects and structural disorder in the amorphous carbon [49]. On the contrary, the sp2 hybridization was enhanced accompanied by the reduction of defects and structural disorder for Fe_3O_4@C-873 (I_D/I_G < 1). This confirmed that the carbon defects and structural disorder were eliminated partially by the crystallization of the amorphous carbon. The defects and structural disorder would lower the electron transfer efficiency, although they benefited from the infiltration of the electrolyte. For further investigation of the microstructure, the isothermal N_2-adsorption/desorption at

77 K was carried out to evaluate the BET surface area and pore structure. For Fe_3O_4@C-873, the BET surface area was approximately 51.4 m^2/g (Figure 3b), and there were abundant mesoporous structures with a main pore size of approximately 3 nm, together with some that were 10 nm, as illustrated in the insert of Figure 3b, which could provide active sites on the surface for the adsorption of the electrolyte [50]. However, the BET surface area of Fe_3O_4@C-773 (Figure 3c) was only 22.4 m^2/g, far lower than the value of Fe_3O_4@C-873, and there was nearly no pore structure, possibly due to its leaves-like nanosheet structure. Certainly, the large surface and pore structure is more favorable to the enhancement of electrolyte entrance and infiltration and, especially, beneficial for Li/Li^+ diffusion [51].

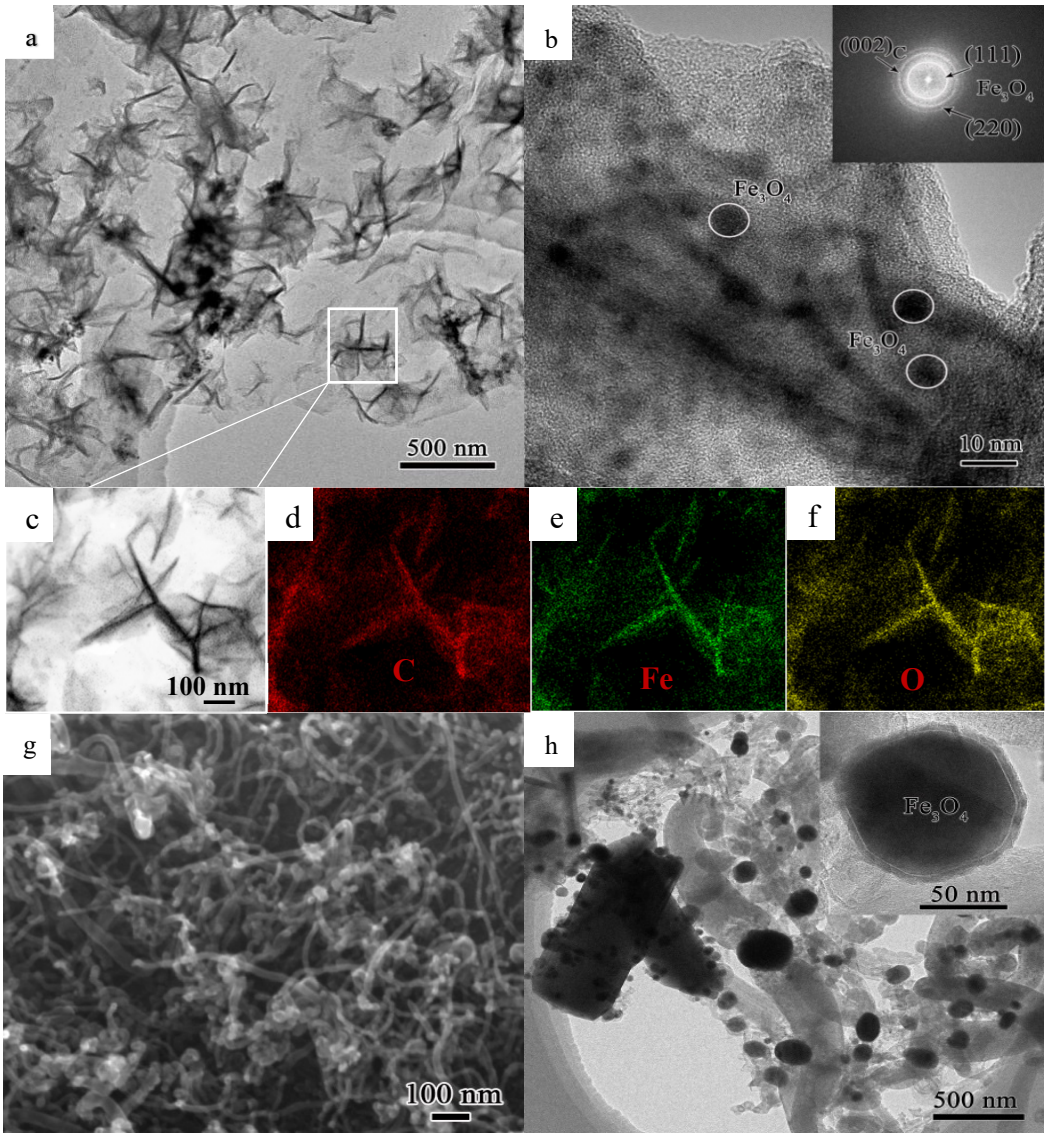

Figure 2. (**a**–**c**) TEM images of Fe_3O_4@C-773; (**d**–**f**) corresponding EDS element mapping signals of the C, Fe, and O elements. (**g**,**h**) TEM images of Fe_3O_4@C-873.

The surface element valence and chemical composition of the Fe_3O_4@C nanocomposites were revealed by XPS analysis. Figure 4 shows the XPS of the Fe_3O_4@C nanocomposites. Figure 4a shows the full XPS spectrum of Fe_3O_4@C-873, in which the existence of Fe, C and O species was verified by the Fe 2p, C 1s and O 1s characteristic peaks. In the fine spectra of Fe 2p (Figure 4b), the peaks centered at approximately 711 and 725 eV, attributed to the characteristic peaks of Fe $2p_{3/2}$ and Fe $2p_{1/2}$, which corresponded to Fe^{3+} and Fe^{2+}, respectively [15,52]. This confirmed the existence of Fe_3O_4. The fine spectrum of C 1s

contained four different peaks at 289.4, 287.0, 285.2 and 284.7 eV, corresponding to O-C=O, C=O, C-O, and C-C/C=C bonds, respectively [15,47,48], as seen in Figure 4c. The weak peaks derived from O-C=O, C=O and C-O bonds could be caused by the interactions of the C and O atoms located in the interface between Fe_3O_4 and carbon, which could be further confirmed by the fine spectrum of O 1s. In the high-resolution XPS spectra of O 1s (Figure 4d), the peak at 530.5 eV was attributed to the Fe-O bond in iron oxide, the other two peaks at 533.9 eV (O-C=O) and 532.0 eV (O-C/O=C) could be ascribed to the chemical bonds between carbon atoms and oxygen-containing groups on the surface of iron oxide [17,53,54]. The emergence of chemical interactions between C and Fe_3O_4 would facilitate the electron transfer between these two phases. For Fe_3O_4@C-773, the XPS analysis results are illustrated in Figure 4e–h. It was similar to Fe_3O_4@C-873, implying they had similar chemical composition and element valence states. Overall, the XPS further confirmed the preparation of Fe_3O_4@C nanocomposites and the existence of chemical interactions between C and Fe_3O_4.

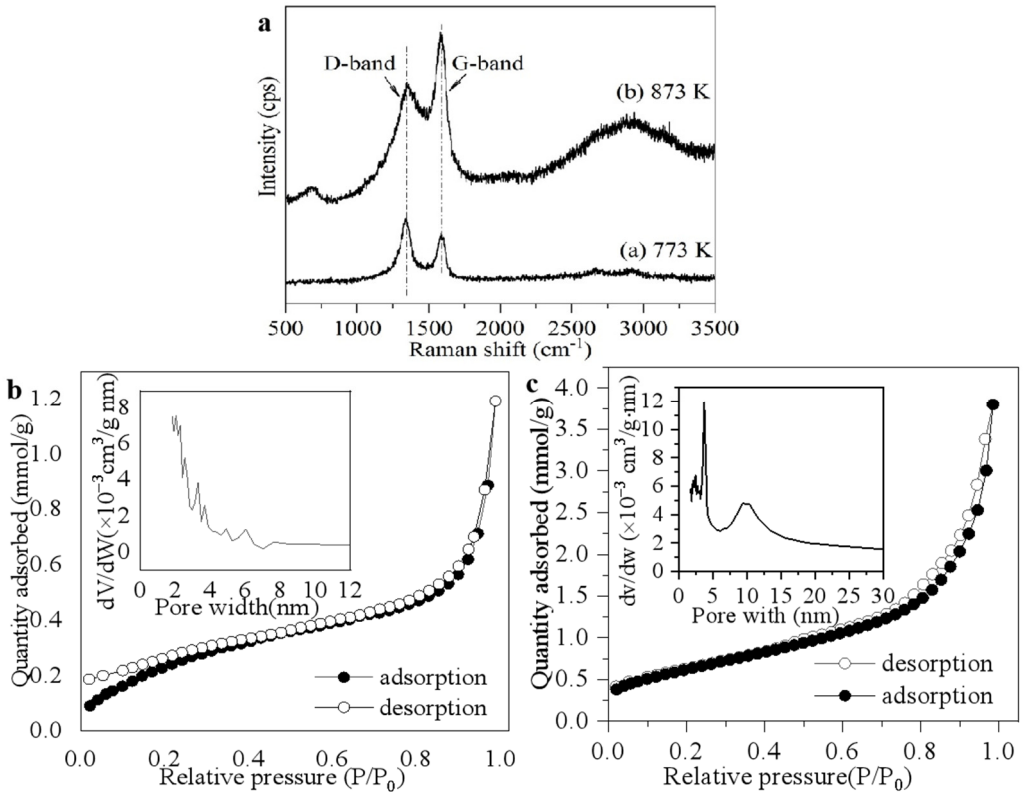

Figure 3. (**a**) Raman spectroscopy; (**b**,**c**): Isothermal N_2-adsorption/desorption curves at 77 K and pore size distribution curve for Fe_3O_4@C-873 (**b**) and Fe_3O_4@C-773 (**c**), respectively.

Figure 5a shows the CV profiles for Fe_3O_4@C-873. Three cathodic peaks (1.63, 0.90 and 0.54 V) were observed in the lithiation process. The peak at 1.63 V could be attributed to the reaction of Li inserting into the lattice of Fe_3O_4 crystalline, which was associated with the reaction [15]:

$$Fe_3O_4 + xLi^+ + xe^- = Li_x(Fe_3O_4)\ (0 \leq x \leq 2) \quad (1)$$

The peak located at 0.90 V could be corresponding to the reduction of Fe^{3+} and Fe^{2+} to Fe^0 and the formation of Li_2O based on the reaction equation [55,56]:

$$Li_x(Fe_3O_4) + (8 - x)Li^+ + (8 - x)e^- = 3Fe + 4Li_2O\ (0 \leq x \leq 2) \quad (2)$$

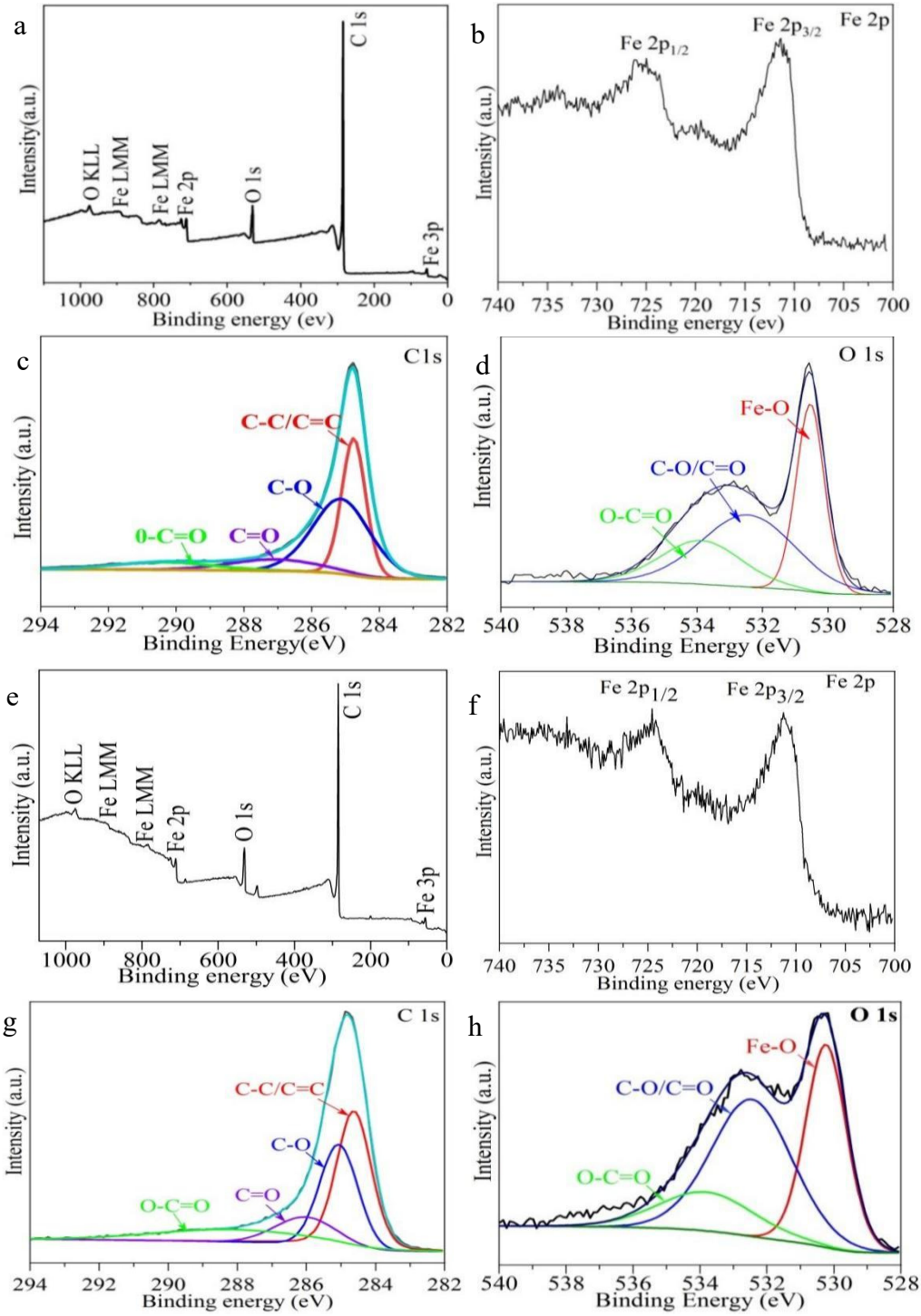

Figure 4. (**a**,**e**) XPS spectrum, (**b**,**f**) Fe 2P XPS spectrum, (**c**,**g**): C 1s XPS spectrum, (**d**,**h**) O 1s XPS spectrum for Fe_3O_4@C-873 and Fe_3O_4@C-773, respectively.

The peak of 0.54 V, which appeared only at the first cycle, was ascribed to the formation of the solid electrolyte interface (SEI) film that was stable in the following charge and discharge procedure [15]. For delithiation, the reduced Fe^0 was gradually oxidized to Fe^{2+} and Fe^{3+}, accompanied by the formation of $Li_x(Fe_3O_4)$ by two anodic steps at 1.70 and 1.94 V, respectively [55–58]. After the first cycle, the CV curves and the position of the peaks almost overlapped in the second and third cycles, implying good charge and discharge reversibility for Fe_3O_4@C-873 as a LIBs anode. For Fe_3O_4@C-773 (Figure 5c), its CV curves were similar to those of Fe_3O_4@C-873. However, the cathodic peaks slightly shifted toward

a higher voltage, indicating better kinetics, which was possibly related to the ultrafine Fe_3O_4 nanoparticles. Figure 5b depicts the discharge and charge curves of Fe_3O_4@C-873 at the current densities of 0.2, 0.5, 1.0, 2.0 and 5.0 A g^{-1}, respectively. For the profile of 0.2 A g^{-1}, there was one plateau at approximately 0.9 V in the discharge process, while there was one plateau containing two transitions at approximately 1.5 and 2.0 V in the charging process, which was consistent with two reaction peaks in the CV profiles; the two transitions corresponded to the oxidation of Fe to Fe^{2+} and Fe^{3+}, respectively. The initial discharge capacity and charge capacity were approximately 986 and 760 mAh g^{-1} at the current density of 0.2 A g^{-1}. The irreversible capacity loss could mainly result from the formation of SEI, the side reaction between the electrode and the electrolyte and the decomposition of the electrolyte [15]. Certainly, the reversible capacity reduced with the increase in discharge/charge current density, but it remained at a relatively high reversible capacity of 576 mAh g^{-1} at 5.0 A g^{-1}. Unfortunately the discharge capacity and charge capacity at 0.2 A g^{-1} were only 587 and 553 mAh g^{-1}, and it was further reduced to 291 mAh g^{-1} when discharging at 5.0 A g^{-1} for Fe_3O_4@C-773 (Figure 5d). That is to say, Fe_3O_4@C-873 had a higher capacity and superior rate performance compared to Fe_3O_4@C-773.

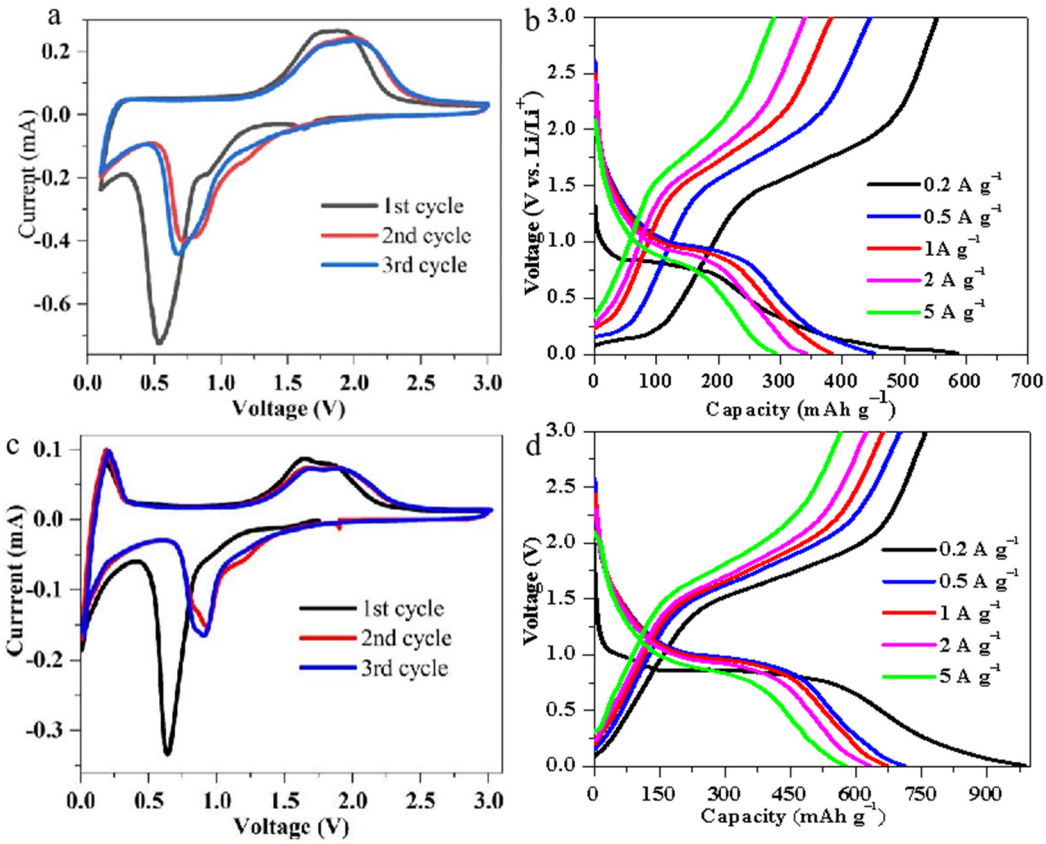

Figure 5. (**a**,**c**) cyclic voltammetry profiles of Fe_3O_4@C-873 and Fe_3O_4@C-773 at a scan rate of 0.1 mV s^{-1}; (**b**,**d**) voltage capacity curves of Fe_3O_4@C-873 and Fe_3O_4@C-773 at different current density (0.2, 0.5, 1, 2 and 5 A g^{-1}).

The Li^+ storage performance of the Fe_3O_4@C electrodes was further systematically evaluated by the extended galvanostatic discharge and charge measurements, as depicted in Figure 6. Figure 6a–d show the cycling stability of Fe_3O_4@C-873 at different current densities. As observed in Figure 6a, the discharge capacity reached 1006 mAh g^{-1} (efficiency: ~98%) from approximately 781 mAh g^{-1} (efficiency: ~92%) after 100 cycles at 0.2 A g^{-1}. The maximum capacity was approximately 921 mAh g^{-1} (efficiency: ~98%) at the 94th cycle and then gradually attenuated to 552 mAh g^{-1} (efficiency: ~100%) after 300 cycles at 0.5 A g^{-1}

(Figure 6b). When the current density further increased to 1 A g^{-1}, it still had a reversible capacity of 423 mAh g^{-1} and 100% efficiency after 500 cycles (Figure 6c). For Fe_3O_4@C-773 (Figure 6e–h), the discharge capacity increased to 662 mAh g^{-1} (efficiency: ~98%) from 525 mA h g^{-1} (efficiency: ~92%) at the 45th cycle and then returned to 526 mAh g^{-1} (efficiency: ~98%) at the 100th cycle under a current density of 0.2 A g^{-1} (Figure 6e). The maximum capacity was approximately 548 mAh g^{-1} (efficiency: ~97%) at the 50th cycle and then reduced to 326 mAh g^{-1} (efficiency: ~100%) after 300 cycles at 0.5 A g^{-1} (Figure 6f). When the discharge/charge current density increased to 1 A g^{-1}, the reversible capacity attenuated to 258 mAh g^{-1} (efficiency: ~100%) after continuous 500 cycles (Figure 6g). According to ref. [59], the capacity of pure Fe_3O_4 was only 126.8 mAh g^{-1} after 100 cycles at 0.1 A g^{-1}. Significantly, the electrochemical properties and cycling stability of Fe_3O_4 were effectively improved by designing the unique structure Fe_3O_4@C nanocomposites. Figure 6d illustrates the rate performance of Fe_3O_4@C-873, which exhibited no capacity decay after 70 discharge and charge cycles in the current density range from 0.2 to 5 A g^{-1}. For example, the discharge capacity was 772 mAh g^{-1} when undergoing 10 cycles at 0.2 A g^{-1}. It was approximately 580 mAh g^{-1} after 50 cycles and the current density increased to 5 A g^{-1}; however, it could reach 978 mAh g^{-1} at the 70th cycle when the current density reduced to 0.2 A g^{-1} again. For Fe_3O_4@C-773 (Figure 6h), it had a similar rate performance; the corresponding capacity was approximately 531, 300 and 655 mAh g^{-1}, respectively. From the experiment results, we could see that two samples, especially Fe_3O_4@C-873, exhibited fairly good cycle stability and excellent rate performance. Certainly, it should be pointed out that Fe_3O_4@C-873 had a significantly higher capacity and better rate performance than Fe_3O_4@C-773. However, Fe_3O_4@C-773 more easily reached the maximum capacity with better kinetics (~50 cycles, less than ~94 cycles for Fe_3O_4@C-873), which could result from its large amount of defects and the superfine Fe_3O_4 nanoparticles, together with the leaves-like amorphous carbon structure, by enhancing the electrolyte absorption and shortening the Li/Li^+ diffusion distance. For Fe_3O_4@C-873, the superior cycling stability and the outstanding high-rate performance were mainly attributed to the improved structural stability of nano-Fe_3O_4 for the robust core-shell structure supported by the nanotube/nanorod crystalline carbon.

For further understanding of the mechanism of the significantly enhanced electrochemical performances, the electrochemical impedance measurements were carried out, and the results are shown in Figure 7a. As depicted in Figure 7b, a corresponding equivalent circuit model was established to analyze the electrochemical impedance spectroscopy. In this model, R_s is the internal resistance of the analog battery (including the electrolyte impedance and the electrode impedance), R_{ct} represents the charge-transfer resistance, CPE_1 is related to the constant phase element, Z_w is the Warburg resistance associated with the Li/Li^+ diffusion in the active materials [55,58–61]. From Figure 7a, it could be observed that the electrochemical impedance spectroscopies for two samples contained only one observable semicircle in the test full frequency range. It was attributed to the interfacial charge transfer (R_{ct}) combined with the double-layer capacitance CPE_1. However, Fe_3O_4@C-873 contained a much smaller semicircle than Fe_3O_4@C-773. The inclined lines in the low-frequency region were derived from the Li^+ diffusion into the Fe_3O_4@C materials. The impedance parameters were achieved by fitting the experimental Nyquist plots (Figure 7a) using the established model in Figure 7b. For Fe_3O_4@C-773, the impedance parameters R_s and R_{ct} were achieved to be approximately 1.2 and 252.1 Ω, respectively. They were 4.0 and 103.0 Ω for Fe_3O_4@C-873. The results indicated that the Rs of Fe_3O_4@C-773 and Fe_3O_4@C-873 were very close, but the Rct of Fe_3O_4@C-773 was far higher than that of Fe_3O_4@C-873, indicating Fe_3O_4@C-873 had better charge transfer property. It could be attributed to the better structural integrity, such as fewer defects and good crystallinity for Fe_3O_4@C-873. The results suggested that the novel structure Fe_3O_4@C-873 nanocomposite had significantly improved electrochemical performances compared with Fe_3O_4.

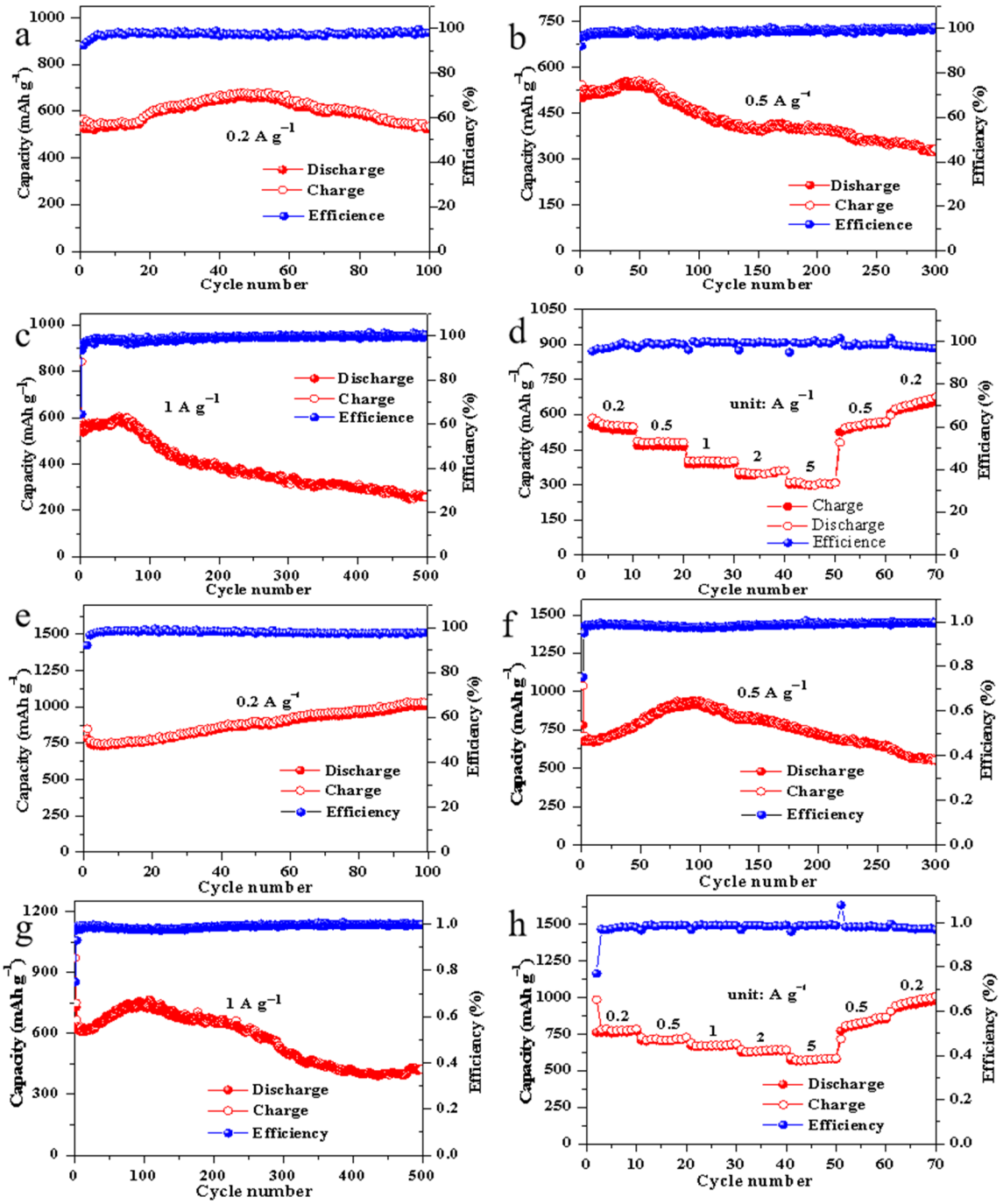

Figure 6. Cycle performances of Fe_3O_4@C-873 (**a**–**c**) and Fe_3O_4@C-773 (**e**–**g**) at various current densities; rate performance of Fe_3O_4@C-873 (**d**) and Fe_3O_4@C-773 (**h**) at various current rates from 0.2 to 5.0 A g^{-1} in the potential range of 0.01~3.0 V (vs. Li/Li^+).

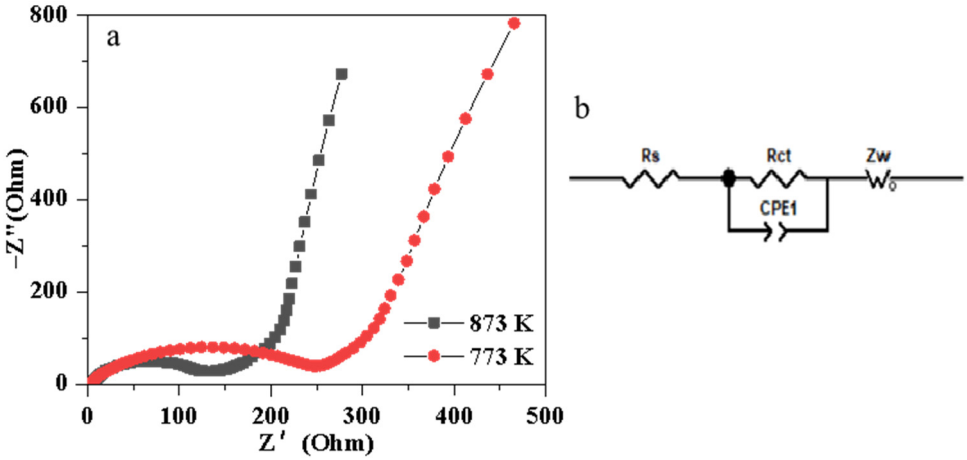

Figure 7. (**a**) electrochemical impedance spectra and (**b**) the corresponding equivalent circuit diagram.

4. Conclusions

In summary, leaves-like amorphous carbon-nanosheet-encapsulated ultrafine Fe_3O_4 nanoparticle composites and carbon nanotube/nanorod-supported core-shell structure Fe_3O_4 nanoparticle composites were fabricated via an in situ encapsulation route, which consists of PA milling the ferrocene ($C_{10}H_{10}Fe$) precursor and subsequent heating treatment. The carbon nanotube/nanorod-supported core-shell structure Fe_3O_4 nanocomposite has a larger specific area (51.4 m^2/g), fewer defects and better crystallinity than the leaves-like amorphous carbon-nanosheet-encapsulated ultrafine Fe_3O_4 nanocomposite (22.4 m^2/g), and the former also contains abundant mesoporous structures. The carbon nanotube/nanorod-supported core-shell structure Fe_3O_4 nanocomposite exhibits outstanding cycling stability and high-rate capability as anode materials for LIBs. Remarkably, it shows 1006 mAh g^{-1} and retains 423 mAh g^{-1} after 500 cycles at 1A g^{-1}. The improved electrochemical performances could be mainly attributed to the synergetic effects of the hierarchical architecture and the nanostructure. This work supplies a feasible route for the preparation of novel structure Fe_3O_4@C nanocomposites as high-performance electrode materials.

Author Contributions: H.Z. and H.L. wrote the main manuscript; W.H., Y.W. and X.Y. performed equal work in preparing the samples and taking the electrochemical measurements; C.J. prepared Figures 5–7; W.Z. performed the XRD analysis; C.L. performed the XPS analysis; L.D. performed the microstructure characterizations (SEM and TEM). X.X. revised the manuscript. All authors have read and agreed to the published version of the manuscript.

Funding: This work was financially supported by the Natural Science Foundation of Fujian Province, China (No. 2021J011209); the Open Fund of Fujian Provincial Key Laboratory of Functional Materials and Applications, Xiamen University of Technology, (fma2020003 and fma2022007).

Data Availability Statement: Not applicable.

Conflicts of Interest: The authors declare no conflict of interest.

References

1. Liu, Y.; Zhu, Y.; Cui, Y. Challenges and Opportunities towards Fast-Charging Battery Materials. *Nat. Energy* **2019**, *4*, 540–550. [CrossRef]
2. Wu, F.; Maier, J.; Yu, Y. Guidelines and Trends for Next-Generation Rechargeable Lithium and Lithium-Ion Batteries. *Chem. Soc. Rev.* **2020**, *49*, 1569–1614. [CrossRef]
3. Shi, Y.; Zhang, J.; Bruck, A.M.; Zhang, Y.; Li, J.; Stach, E.A.; Takeuchi, K.J.; Marschilok, A.C.; Takeuchi, E.S.; Yu, G. A Tunable 3D Nanostructured Conductive Gel Framework Electrode for High-Performance Lithium Ion Batteries. *Adv. Mater.* **2017**, *29*, 1603922. [CrossRef]
4. Goodenough, J.B. Evolution of Strategies for Modern Rechargeable Batteries. *Acc. Chem. Res.* **2013**, *46*, 1053–1061. [CrossRef]

5. Zheng, H.; Xu, H.-S.; Hu, J.; Liu, H.; Wei, L.; Wu, S.; Huang, Y.; Li, J.; Tang, K. Construction of Hierarchical MnSe@$SnSe_2$@N–C Nanorods for High-Performance Lithium-Ion Batteries. *ACS Appl. Energy Mater.* **2022**, *5*, 6586–6596. [CrossRef]
6. Liu, J.; Yu, L.; Wu, C.; Wen, Y.; Yin, K.; Chiang, F.-K.; Hu, R.; Liu, J.; Sun, L.; Gu, L.; et al. New Nanoconfined Galvanic Replacement Synthesis of Hollow Sb@C Yolk–Shell Spheres Constituting a Stable Anode for High-Rate Li/Na-Ion Batteries. *Nano Lett.* **2017**, *17*, 2034–2042. [CrossRef]
7. Li, X.; Dhanabalan, A.; Gu, L.; Wang, C. Three-Dimensional Porous Core-Shell Sn@Carbon Composite Anodes for High-Performance Lithium-Ion Battery Applications. *Adv. Energy Mater.* **2012**, *2*, 238–244. [CrossRef]
8. Yu, L.; Liu, J.; Xu, X.; Zhang, L.; Hu, R.; Liu, J.; Yang, L.; Zhu, M. Metal–Organic Framework-Derived NiSb Alloy Embedded in Carbon Hollow Spheres as Superior Lithium-Ion Battery Anodes. *ACS Appl. Mater. Interfaces* **2017**, *9*, 2516–2525. [CrossRef]
9. Zhang, H.; Hu, R.; Liu, H.; Sun, W.; Lu, Z.; Liu, J.; Yang, L.; Zhang, Y.; Zhu, M. A Spherical Sn–Fe_3O_4@graphite Composite as a Long-Life and High-Rate-Capability Anode for Lithium Ion Batteries. *J. Mater. Chem. A* **2016**, *4*, 10321–10328. [CrossRef]
10. Hao, S.; Zhang, B.; Wang, Y.; Li, C.; Feng, J.; Ball, S.; Srinivasan, M.; Wu, J.; Huang, Y. Hierarchical Three-Dimensional Fe_3O_4@porous Carbon Matrix/Graphene Anodes for High Performance Lithium Ion Batteries. *Electrochim. Acta* **2018**, *260*, 965–973. [CrossRef]
11. Marzuki, N.S.; Taib, N.U.; Hassan, M.F.; Idris, N.H. Enhanced Lithium Storage in Co_3O_4/Carbon Anode for Li-Ion Batteries. *Electrochim. Acta* **2015**, *182*, 452–457. [CrossRef]
12. Kim, W.-S.; Hwa, Y.; Kim, H.-C.; Choi, J.-H.; Sohn, H.-J.; Hong, S.-H. SnO_2@Co_3O_4 Hollow Nano-Spheres for a Li-Ion Battery Anode with Extraordinary Performance. *Nano Res.* **2014**, *7*, 1128–1136. [CrossRef]
13. Zhao, Y.; Liu, C.; Yi, R.; Li, Z.; Chen, Y.; Li, Y.; Mitrovic, I.; Taylor, S.; Chalker, P.; Yang, L.; et al. Facile Preparation of Co_3O_4 Nanoparticles Incorporating with Highly Conductive MXene Nanosheets as High-Performance Anodes for Lithium-Ion Batteries. *Electrochim. Acta* **2020**, *345*, 136203. [CrossRef]
14. Zhao, M.-Q.; Torelli, M.; Ren, C.E.; Ghidiu, M.; Ling, Z.; Anasori, B.; Barsoum, M.W.; Gogotsi, Y. 2D Titanium Carbide and Transition Metal Oxides Hybrid Electrodes for Li-Ion Storage. *Nano Energy* **2016**, *30*, 603–613. [CrossRef]
15. Li, L.; Kovalchuk, A.; Fei, H.; Peng, Z.; Li, Y.; Kim, N.D.; Xiang, C.; Yang, Y.; Ruan, G.; Tour, J.M. Enhanced Cycling Stability of Lithium-Ion Batteries Using Graphene-Wrapped Fe_3O_4-Graphene Nanoribbons as Anode Materials. *Adv. Energy Mater.* **2015**, *5*, 1500171. [CrossRef]
16. Ma, F.-X.; Hu, H.; Wu, H.B.; Xu, C.-Y.; Xu, Z.; Zhen, L.; David Lou, X.W. Formation of Uniform Fe_3O_4 Hollow Spheres Organized by Ultrathin Nanosheets and Their Excellent Lithium Storage Properties. *Adv. Mater.* **2015**, *27*, 4097–4101. [CrossRef]
17. Li, Z.; Hu, X.; Li, B.; Wang, X.; Shi, Z.; Lu, J.; Wang, Z. MOF-Derived Fe_3O_4 Hierarchical Nanocomposites Encapsulated by Carbon Shells as High-Performance Anodes for Li-Storage Systems. *J. Alloys Compd.* **2021**, *875*, 159906. [CrossRef]
18. Hu, X.; Ma, M.; Zeng, M.; Sun, Y.; Chen, L.; Xue, Y.; Zhang, T.; Ai, X.; Mendes, R.G.; Rümmeli, M.H.; et al. Supercritical Carbon Dioxide Anchored Fe_3O_4 Nanoparticles on Graphene Foam and Lithium Battery Performance. *ACS Appl. Mater. Interfaces* **2014**, *6*, 22527–22533. [CrossRef]
19. Bulut Kopuklu, B.; Tasdemir, A.; Alkan Gursel, S.; Yurum, A. High Stability Graphene Oxide Aerogel Supported Ultrafine Fe_3O_4 Particles with Superior Performance as a Li-Ion Battery Anode. *Carbon* **2021**, *174*, 158–172. [CrossRef]
20. Li, L.; Wang, H.; Xie, Z.; An, C.; Jiang, G.; Wang, Y. 3D Graphene-Encapsulated Nearly Monodisperse Fe_3O_4 Nanoparticles as High-Performance Lithium-Ion Battery Anodes. *J. Alloys Compd.* **2020**, *815*, 152337. [CrossRef]
21. Mao, J.; Niu, D.; Zheng, N.; Jiang, G.; Zhao, W.; Shi, J.; Li, Y. Fe_3O_4 -Embedded and N-Doped Hierarchically Porous Carbon Nanospheres as High-Performance Lithium Ion Battery Anodes. *ACS Sustain. Chem. Eng.* **2019**, *7*, 3424–3433. [CrossRef]
22. Yao, J.; Zhang, K.; Wang, W.; Zuo, X.; Yang, Q.; Tang, H.; Wu, M.; Li, G. Remarkable Enhancement in the Photoelectric Performance of Uniform Flower-like Mesoporous Fe_3O_4 Wrapped in Nitrogen-Doped Graphene Networks. *ACS Appl. Mater. Interfaces* **2018**, *10*, 19564–19572. [CrossRef]
23. Guo, Y.; Zhang, D.; Yang, Y.; Wang, Y.; Bai, Z.; Chu, P.K.; Luo, Y. MXene-Encapsulated Hollow Fe_3O_4 Nanochains Embedded in N-Doped Carbon Nanofibers with Dual Electronic Pathways as Flexible Anodes for High-Performance Li-Ion Batteries. *Nanoscale* **2021**, *13*, 4624–4633. [CrossRef]
24. Liu, J.; Xu, X.; Hu, R.; Yang, L.; Zhu, M. Uniform Hierarchical Fe_3O_4 @Polypyrrole Nanocages for Superior Lithium Ion Battery Anodes. *Adv. Energy Mater.* **2016**, *6*, 1600256. [CrossRef]
25. Li, H.; Wang, J.; Li, Y.; Zhao, Y.; Tian, Y.; Kurmanbayeva, I.; Bakenov, Z. Hierarchical Sandwiched Fe_3O_4@C/Graphene Composite as Anode Material for Lithium-Ion Batteries. *J. Electroanal. Chem.* **2019**, *847*, 113240. [CrossRef]
26. Yan, Z.; Jiang, X.; Dai, Y.; Xiao, W.; Li, X.; Du, N.; He, G. Pulverization Control by Confining Fe_3O_4 Nanoparticles Individually into Macropores of Hollow Carbon Spheres for High-Performance Li-Ion Batteries. *ACS Appl. Mater. Interfaces* **2018**, *10*, 2581–2590. [CrossRef]
27. Li, M.; Du, H.; Kuai, L.; Huang, K.; Xia, Y.; Geng, B. Scalable Dry Production Process of a Superior 3D Net-Like Carbon-Based Iron Oxide Anode Material for Lithium-Ion Batteries. *Angew. Chem. Int. Ed.* **2017**, *56*, 12649–12653. [CrossRef]
28. Park, G.D.; Hong, J.H.; Jung, D.S.; Lee, J.-H.; Kang, Y.C. Unique Structured Microspheres with Multishells Comprising Graphitic Carbon-Coated Fe_3O_4 Hollow Nanopowders as Anode Materials for High-Performance Li-Ion Batteries. *J. Mater. Chem. A* **2019**, *7*, 15766–15773. [CrossRef]
29. Wang, L.; Liu, F.; Pal, A.; Ning, Y.; Wang, Z.; Zhao, B.; Bradley, R.; Wu, W. Ultra-Small Fe_3O_4 Nanoparticles Encapsulated in Hollow Porous Carbon Nanocapsules for High Performance Supercapacitors. *Carbon* **2021**, *179*, 327–336. [CrossRef]

30. Ding, R.; Zhang, J.; Qi, J.; Li, Z.; Wang, C.; Chen, M. N-Doped Dual Carbon-Confined 3D Architecture RGO/Fe_3O_4/AC Nanocomposite for High-Performance Lithium-Ion Batteries. *ACS Appl. Mater. Interfaces* **2018**, *10*, 13470–13478. [CrossRef]
31. Wei, W.; Yang, S.; Zhou, H.; Lieberwirth, I.; Feng, X.; Müllen, K. 3D Graphene Foams Cross-Linked with Pre-Encapsulated Fe_3O_4 Nanospheres for Enhanced Lithium Storage. *Adv. Mater.* **2013**, *25*, 2909–2914. [CrossRef]
32. Liu, H.; Jia, M.; Zhu, Q.; Cao, B.; Chen, R.; Wang, Y.; Wu, F.; Xu, B. 3D-0D Graphene-Fe_3O_4 Quantum Dot Hybrids as High-Performance Anode Materials for Sodium-Ion Batteries. *ACS Appl. Mater. Interfaces* **2016**, *8*, 26878–26885. [CrossRef]
33. Qin, X.; Zhang, H.; Wu, J.; Chu, X.; He, Y.-B.; Han, C.; Miao, C.; Wang, S.; Li, B.; Kang, F. Fe_3O_4 Nanoparticles Encapsulated in Electrospun Porous Carbon Fibers with a Compact Shell as High-Performance Anode for Lithium Ion Batteries. *Carbon* **2015**, *87*, 347–356. [CrossRef]
34. Duan, Y.; Zhang, B.; Zheng, J.; Hu, J.; Wen, J.; Miller, D.J.; Yan, P.; Liu, T.; Guo, H.; Li, W.; et al. Excess Li-Ion Storage on Reconstructed Surfaces of Nanocrystals To Boost Battery Performance. *Nano Lett.* **2017**, *17*, 6018–6026. [CrossRef]
35. Jiao, J.; Qiu, W.; Tang, J.; Chen, L.; Jing, L. Synthesis of Well-Defined Fe_3O_4 Nanorods/N-Doped Graphene for Lithium-Ion Batteries. *Nano Res.* **2016**, *9*, 1256–1266. [CrossRef]
36. Xiao, Z.; Xia, Y.; Ren, Z.; Liu, Z.; Xu, G.; Chao, C.; Li, X.; Shen, G.; Han, G. Facile Synthesis of Single-Crystalline Mesoporous α-Fe_2O_3 and Fe_3O_4 Nanorods as Anode Materials for Lithium-Ion Batteries. *J. Mater. Chem.* **2012**, *22*, 20566. [CrossRef]
37. Kwon, Y.H.; Park, J.J.; Housel, L.M.; Minnici, K.; Zhang, G.; Lee, S.R.; Lee, S.W.; Chen, Z.; Noda, S.; Takeuchi, E.S.; et al. Carbon Nanotube Web with Carboxylated Polythiophene "Assist" for High-Performance Battery Electrodes. *ACS Nano* **2018**, *12*, 3126–3139. [CrossRef]
38. Gao, T.; Xu, C.; Li, R.; Zhang, R.; Wang, B.; Jiang, X.; Hu, M.; Bando, Y.; Kong, D.; Dai, P.; et al. Biomass-Derived Carbon Paper to Sandwich Magnetite Anode for Long-Life Li-Ion Battery. *ACS Nano* **2019**, *13*, 11901–11911. [CrossRef]
39. Wang, Y.; Chen, L.; Liu, H.; Xiong, Z.; Zhao, L.; Liu, S.; Huang, C.; Zhao, Y. Cornlike Ordered N-Doped Carbon Coated Hollow Fe_3O_4 by Magnetic Self-Assembly for the Application of Li-Ion Battery. *Chem. Eng. J.* **2019**, *356*, 746–755. [CrossRef]
40. Wang, B.; Zhang, X.; Liu, X.; Wang, G.; Wang, H.; Bai, J. Rational Design of Fe_3O_4@C Yolk-Shell Nanorods Constituting a Stable Anode for High-Performance Li/Na-Ion Batteries. *J. Colloid Interface Sci.* **2018**, *528*, 225–236. [CrossRef]
41. Xu, X.; Liu, J.; Liu, Z.; Shen, J.; Hu, R.; Liu, J.; Ouyang, L.; Zhang, L.; Zhu, M. Robust Pitaya-Structured Pyrite as High Energy Density Cathode for High-Rate Lithium Batteries. *ACS Nano* **2017**, *11*, 9033–9040. [CrossRef]
42. Liu, Z.; Yu, X.-Y.; Paik, U. Etching-in-a-Box: A Novel Strategy to Synthesize Unique Yolk-Shelled Fe_3O_4 @Carbon with an Ultralong Cycling Life for Lithium Storage. *Adv. Energy Mater.* **2016**, *6*, 1502318. [CrossRef]
43. Guo, W.; Sun, W.; Lv, L.-P.; Kong, S.; Wang, Y. Microwave-Assisted Morphology Evolution of Fe-Based Metal–Organic Frameworks and Their Derived Fe_2O_3 Nanostructures for Li-Ion Storage. *ACS Nano* **2017**, *11*, 4198–4205. [CrossRef]
44. Du, J.; Tang, Y.; Wang, Y.; Shi, P.; Fan, J.; Xu, Q.; Min, Y. A MOF-Derived Method to Construct Well-Arranged Porous Nanosheets for Lithium Ion Batteries. *Dalton Trans.* **2018**, *47*, 7571–7577. [CrossRef]
45. Dai, R.; Sun, W.; Wang, Y. Ultrasmall Tin Nanodots Embedded in Nitrogen-Doped Mesoporous Carbon: Metal-Organic-Framework Derivation and Electrochemical Application as Highly Stable Anode for Lithium Ion Batteries. *Electrochim. Acta* **2016**, *217*, 123–131. [CrossRef]
46. Wu, L.; Liu, Y.; Zhao, H.; Wang, Z.; Zhu, B.; Zhang, X.; He, P.; Liu, Y.; Yang, T. MOF-Derived Long Spindle-like Carbon-Coated Ternary Transition-Metal-Oxide Composite for Lithium Storage. *ACS Omega* **2022**, *7*, 16837–16846. [CrossRef]
47. Ferrari, A.C.; Robertson, J. Raman spectroscopy in carbons: From nanotubes to diamond-Preface. *Philos. Trans. R. Soc. Lond. Ser. Math. Phys. Eng. Sci.* **2004**, *362*, 2269–2270. [CrossRef]
48. Lv, L.-P.; Du, P.; Liu, P.; Li, X.; Wang, Y. Integrating Mixed Metallic Selenides/Nitrogen-Doped Carbon Heterostructures in One-Dimensional Carbon Fibers for Efficient Oxygen Reduction Electrocatalysis. *ACS Sustain. Chem. Eng.* **2020**, *8*, 8391–8401. [CrossRef]
49. Duan, H.; Zhang, S.; Chen, Z.; Xu, A.; Zhan, S.; Wu, S. Self-Formed Channel Boosts Ultrafast Lithium Ion Storage in Fe_3O_4@Nitrogen-Doped Carbon Nanocapsule. *ACS Appl. Mater. Interfaces* **2020**, *12*, 527–537. [CrossRef]
50. Xie, Y.; Qiu, Y.; Tian, L.; Liu, T.; Su, X. Ultrafine Hollow Fe_3O_4 Anode Material Modified with Reduced Graphene Oxides for High-Power Lithium-Ion Batteries. *J. Alloys Compd.* **2022**, *894*, 162384. [CrossRef]
51. Pan, Q.; Ding, Y.; Yan, Z.; Cai, Y.; Zheng, F.; Huang, Y.; Wang, H.; Li, Q. Designed Synthesis of Fe_3O_4@NC Yolk-Shell Hollow Spheres as High Performance Anode Material for Lithium-Ion Batteries. *J. Alloys Compd.* **2020**, *821*, 153569. [CrossRef]
52. Yuan, M.; Zhao, Y.; Sun, Z.; Bakenov, Z. Rational Design of MOFs-Derived Fe_3O_4@C Interwoven with Carbon Nanotubes as Sulfur Host for Advanced Lithium-sulfur Batteries. *J. Electroanal. Chem.* **2020**, *877*, 114608. [CrossRef]
53. Kumar, R.; Singh, R.K.; Vaz, A.R.; Savu, R.; Moshkalev, S.A. Self-Assembled and One-Step Synthesis of Interconnected 3D Network of Fe_3O_4/Reduced Graphene Oxide Nanosheets Hybrid for High-Performance Supercapacitor Electrode. *ACS Appl. Mater. Interfaces* **2017**, *9*, 8880–8890. [CrossRef]
54. Yi, Q.; Du, M.; Shen, B.; Ji, J.; Dong, C.; Xing, M.; Zhang, J. Hollow Fe_3O_4/Carbon with Surface Mesopores Derived from MOFs for Enhanced Lithium Storage Performance. *Sci. Bull.* **2020**, *65*, 233–242. [CrossRef]
55. Ma, T.; Liu, X.; Sun, L.; Xu, Y.; Zheng, L.; Zhang, J. Strongly Coupled N-Doped Carbon/Fe_3O_4/N-Doped Carbon Hierarchical Micro/Nanostructures for Enhanced Lithium Storage Performance. *J. Energy Chem.* **2019**, *34*, 43–51. [CrossRef]

56. Cong, B.; Hu, Y.; Sun, S.; Wang, Y.; Wang, B.; Kong, H.; Chen, G. Metal–Organic Framework Derived Amorphous VO_x Coated Fe_3O_4/C Hierarchical Nanospindle as Anode Material for Superior Lithium-Ion Batteries. *Nanoscale* **2020**, *12*, 16901–16909. [CrossRef]
57. Huang, J.; Dai, Q.; Cui, C.; Ren, H.; Lu, X.; Hong, Y.; Woo Joo, S. Cake-like Porous Fe_3O_4@C Nanocomposite as High-Performance Anode for Li-Ion Battery. *J. Electroanal. Chem.* **2022**, *918*, 116508. [CrossRef]
58. Zhang, S.S.; Xu, K.; Jow, T.R. EIS Study on the Formation of Solid Electrolyte Interface in Li-Ion Battery. *Electrochim. Acta* **2006**, *51*, 1636–1640. [CrossRef]
59. Moss, P.L.; Au, G.; Plichta, E.J.; Zheng, J.P. Investigation of Solid Electrolyte Interfacial Layer Development during Continuous Cycling Using Ac Impedance Spectra and Micro-Structural Analysis. *J. Power Sources* **2009**, *189*, 66–71. [CrossRef]
60. Kang, L.; Zhang, M.; Zhang, J.; Liu, S.; Zhang, N.; Yao, W.; Ye, Y.; Luo, C.; Gong, Z.; Wang, C. Dual-defect surface engineering of bimetallic sulfide nanotubes towards flexible asymmetric solid-state supercapacitors. *J. Mater. Chem. A* **2020**, *8*, 24053–24064. [CrossRef]
61. Liu, S.; Kang, L.; Zhang, J.; Jung, E.; Lee, S.; Jun, S.C. Structural engineering and surface modification of MOF-derived cobalt-based hybrid nanosheets for flexible solid-state supercapacitors. *Energy Storage Mater.* **2020**, *32*, 167–177. [CrossRef]

Disclaimer/Publisher's Note: The statements, opinions and data contained in all publications are solely those of the individual author(s) and contributor(s) and not of MDPI and/or the editor(s). MDPI and/or the editor(s) disclaim responsibility for any injury to people or property resulting from any ideas, methods, instructions or products referred to in the content.